Impact of Supraparticle Sizes and Morphology on Interparticle Spacing, Slurry Rheology, Coating Density, and Electrochemical Performance in Si/C Anodes for Li-Ion Batteries

Adil Amin [a], Moritz Loewenich [b], Lars Grebener [a], Mohaned Hammad [a], Simon Heckenbach [a], Mena-Alexander Kräenbring [a], Ahammad Suhail Odungat [a], Atharva Harshawardhan Ladole [b], Thai Binh Nguyen [c,d], Daniel Schwabenland [b], Hasan Kadah Salim [a], Hartmut Wiggers [b,c], Doris Segets [a,c] and Fatih Özcan [a,c*]

[a] *Institute for Energy and Materials Processes – Particle Science and Technology (EMPI – PST), University of Duisburg-Essen (UDE), Carl-Benz-Straße 199, 47057 Duisburg, Germany*

[b] *Institute for Energy and Materials Processes – Reactive Fluids (EMPI – RF), University of Duisburg-Essen (UDE), Carl-Benz-Straße 199, 47057 Duisburg, Germany*

[c] *Center for Nanointegration Duisburg-Essen (CENIDE), University of Duisburg-Essen (UDE), Carl-Benz-Straße 199, 47057 Duisburg, Germany*

[d] *Interdisciplinary Center for Analytics on the Nanoscale (ICAN), University of Duisburg-Essen (UDE), Carl-Benz-Straße 199, 47057 Duisburg, Germany*

[*]Email: fatih.oezcan@uni-due.de

Abstract

This study investigates the influence of supraparticle sizes on the performance of Silicon/Carbon (Si/C) composite anodes for lithium-ion batteries. Supraparticles, hierarchically structured agglomerates produced via spray drying, enhance the processability of Si/C nanoparticles by improving handling, packing efficiency, and minimizing solid electrolyte interphase formation. We systematically explore how supraparticle size distributions and associated morphologies affect interparticle spacing, slurry rheology, coating density, and electrochemical performance. Medium-sized supraparticles (5.0–6.0 µm) with spherical shapes exhibit optimal properties, achieving the highest coating density (0.90 g cm^{-3}) and providing precise control over layer thickness and porosity, resulting in uniform coatings. These supraparticles also deliver superior electrochemical performance, with a first-formation Coulombic efficiency of 87.5% and stable cycling, retaining 86.2% of capacity (relative to the third cycle) after 100 cycles. In comparison, smaller supraparticles (irregular shapes) exhibit increased interparticle spacing, resulting in less dense layers and higher SEI formation. These findings highlight the critical role of controlling supraparticle size and morphology to optimize electrode processing and performance, enabling scalable, high-performance energy storage solutions.

1. Introduction

With global temperatures rising and sea levels increasing, the urgency to tackle climate change has never been clearer.[1] Among the various technologies that contribute to this effort, high-energy-density lithium-ion batteries are increasingly recognized for their potential. These batteries can enable electronic devices and vehicles to operate for longer periods between charges, while also occupying less space and weight.[2,3] These batteries play an important role in reducing our reliance on fossil fuels, thus contributing to a more sustainable and environmentally friendly future.[4,5] Silicon (Si), with its high theoretical lithiation capacity, has the potential to replace graphite anodes in conventional lithium-ion batteries.[3,6,7] However, its commercialization is slowed down by significant volume changes during cycling. These volume changes result in (coarse) particle cracking, loss of electrical contacts, electrode delamination and unstable SEI leading to fast capacity decay.[8,9] Nanoparticles have solved the particle cracking[10] issue but inherently suffer from low first cycle Coulombic efficiency (CE)[11] and difficulty in processing Si-dominant (graphite-free) slurries into homogenous-electrodes.[12]

To address the challenge of low first CE, layer delamination and processing challenges associated with incorporating nanoparticles into conventional manufacturing processes, we have recently proposed a post-synthesis spray drying method to produce hierarchically structured secondary particles, termed supraparticles, from gas-phase-synthesized nanoparticles.[13] The concept of hierarchical structuring by spray drying nanomaterials to µm-sized supraparticles is rather new in the field of battery research [14] and enables improved handling properties, like enhanced flowability, reduced dust formation, and easier dispersion. Additionally, it enables the possibility of denser packed electrodes. Additionally, it enables the possibility of denser packed electrodes. Simultaneously, during electrochemical utilization, hierarchical structuring reduces the direct interface area between the active material and the electrolyte. This reduction contributes to a decrease in irreversible reactions during the

formation of the SEI.[13] Furthermore, this structuring helps alleviate stresses from the significant volume expansion of the electrode, stabilizing the layer and enhancing overall battery performance.[9,13,15,16]

However, the mentioned benefits depend on the size and morphology (shape, surface roughness, internal structure and surface area) of the supraparticles, their associated layer porosity, and their stability, particularly against mechanical stress that occurs during slurry processing and cycling in a battery. Therefore, this study investigates how the sizes, associated morphology, and size distributions of supraparticles affect anode manufacturing, from initial slurry preparation to electrode coating and electrochemical performance. As nanomaterial, Si/C composite particles were chosen because of their good electrochemical performance potential[17] and our preliminary proof of principle.[13] We assessed the whole process chain starting from analyzing the supraparticle powder properties, their slurry rheology, the adhesion strength of the generated anodes after coating and drying to the current collector, and finally the fracture-failure mode (adhesive vs cohesive failure) of the generated electrodes and their electrochemical performance. In this way, we were able to examine and comprehend how the supraparticle sizes, associated morphology, size distributions, and their linked porosity impact the properties of the negative electrodes in Li-ion batteries.

2. Experimental and characterizations

2.1. Supraparticles production

As feed material for supraparticles, amorphous Si/C nanoparticles with 4 wt.% carbon were produced by a gas-phase process as described elsewhere (see additional details in SI, Section 1.1),[10,18] yielding nanoparticles in the form of partly sintered aggregates, with primary particle sizes ranging from 100 to 250 nm and average aggregate sizes of approximately 550 nm (Figure S1). The carbon distribution within these particles is uniform at the atomic level, with lower carbon concentration in the center and higher concentration on the primary particle surface,

enhancing their stability during lithiation and improving electrical conductivity. This amorphous nature of Si/C allows homogeneous volume expansion and contraction on Li insertion and extraction, preventing pulverization of the primary particles up to at least 870 nm in size.[19]

For supraparticle formation, the supraparticle size distribution was adjusted by controlling the gas-to-liquid ratio (GLR) in the spray dryer, which is the ratio of the relative volume flow rates of spray-gas (nitrogen) and liquid feed. This was done while keeping other parameters constant: dispersion solid content (3 wt.% Si/C), liquid feed flow rate (0.3 l h^{-1}), drying gas flow rate (35000 l h^{-1}), drying temperature (150 °C), and nozzle diameter (0.7 mm). Four N_2 spray gas flow rates (355, 439, 667, and 1052 l h^{-1}) were used to achieve GLRs of 1.1k, 1.5k, 2.2k, and 3.3k (number in engineering notations, k represents 10^3) to adjust the supraparticle diameter, as it directly influences atomization of the dispersion into small, fast-drying droplets. Details of the mechanism of the spray drying process for a dispersion can be found elsewhere.[13]

2.2. Electrodes preparation

Electrodes for electrochemical testing were prepared using a slurry composed of Si/C supraparticles, conductive carbon, and polyacrylic acid (PAA) as the binder. MiliporeQ water (resistivity of 18.2 MΩ·cm at 25 °C) was selected as the solvent for its environmental benefits, such as being non-toxic and eco-friendly, as well as its lower boiling point which facilitates faster drying.[20] Additionally, it was chosen for its excellent compatibility with PAA, ensuring effective solubilization and stable slurry formation.[21] These were coated onto copper foil, dried (24 h), and punched into 12 mm sized disks for testing (see details in SI, Section 1.2). All electrodes had a mass loading of approximately 0.9 mg cm^{-2}. Half-cells were assembled (see details in SI, Section 1.3) using Si/C working electrodes and a lithium metal counter electrode with 1 M $LiPF_6$ in EC/DMC (1:1) electrolyte and 5 wt.% fluoroethylene carbonate as

electrolyte additive. Electrochemical performance was assessed at 0.5 C between 0.01-1.2 V *vs.* Li/Li^+ after formation cycles at 0.05 C and 0.1 C.

2.3. Characterizations

Supraparticles were characterized using scanning electron microscopy (SEM, Philips XL20, Thermo Fisher) for their morphology, analytical centrifugation (LUMiSizer 6514-44, LUM GmbH) for assessing the supraparticle size distribution of dispersed particles in milli-Q water, N_2 adsorption analysis (Autosorb iQ, Quantachrome Instruments), and mercury intrusion porosimetry (MIP, PoreMaster 60GT, Anton Paar) for determining the specific surface area and pore size distribution, respectively. The stability of Si/C dispersions in water against sedimentation was evaluated by plotting transmittograms using data obtained from an analytical centrifuge (LUMisizer 6514–44, LUM GmbH). To assess the slurry properties, rheological measurements were performed using an MCR 102 (Anton Paar). Anton Paar Germany GmbH, Germany) was studied. Atomic force microscopy (AFM, TOSCA 400, Anton Paar, Germany) was used to characterize the surface topography of the coating, offering detailed insights into the stability of supraparticles and the roughness of the coatings. For measurement of coating thickness, a mechanical screw gauge was used. Adhesion strength and failure mode of coated electrodes (cohesive vs. adhesive break) were analyzed by centrifugal adhesion testing (LUMiFrac 200, LUM GmbH). All methods are described in detail in SI, Section 2.

2.4. Samples overview

Table 1. Overview of the supraparticle powder samples analyzed in this study. The first column lists the naming conventions used for supraparticles of various sizes, as detailed in the second column. The third column indicates the corresponding section numbers where these supraparticles are discussed in the text.

Supraparticles	Median particle size	Discussion section
Large, medium and small	7.5, 5.0, 3.3, 2.0 µm	Manuscript: Section 3.1-3.6 and supporting information
Largest, medium and small	8.5, 6.0, 2.5, 2.2 µm	Figure 1, Section 3.6 and Figure S12

3. Results and discussion

3.1. Supraparticle size distribution control

Spray gas and feed flow rates primarily control the droplet size in the Büchi B-290 spray dryer.[22] For this study, we varied the spray gas flow rate to produce different size distributions of Si/C supraparticles, keeping other parameters (feed concentration, drying gas temperature, and feed flow rate) constant.

As shown in Figure 1a, the cumulative particle size distributions of supraparticle powders produced at different GLRs (1.1k, 1.5k, 2.2k and 3.3k) were measured using analytical centrifugation. The size distributions represent eight supraparticle powders with varying median sizes (colored fields indicate the margin of deviation after repeated spray drying experiments). Among these, the powders with median sizes of 7.5, 5.0, 3.3, and 2.0 µm are discussed extensively throughout this manuscript, focusing on their morphology (e.g., shape, pore structure, and surface area), slurry rheology, electrode density, and electrochemical performance. Additional powders with median sizes of 8.5, 6.0, 2.5, and 2.2 µm, whose curves are also shown in Figure 1a, are compared to the primary powders to emphasize the importance

of powder quality control. As we found the electrochemical performance being sensitive against changes in the powder (Section 3.6), we want to explicitly stress this here.

At a GLR of 1.1k, the supraparticles exhibit a broad size distribution (~0.5 to 15 µm) with an $x_{90,3}$ value of 13.0 µm. As GLR increases, the size distribution shifts to smaller diameters, with $x_{90,3}$ values of 9.0 µm, 4.5 µm, and 3.7 µm for GLRs of 1.5k, 2.2k, and 3.3k, respectively.

Figure 1b shows how the overall median particle size ($x_{50,3}$) of the supraparticle powders (as presented in Figure 1a) depends on the GLRs. The median supraparticle size ($x_{50,3}$) decreased exponentially from 8.0 µm at a GLR of 1.1k to 2.2 µm at 3.3k (Figure 1b), supporting the established trend in the literature of size reduction with increasing GLR.[23,24] SEM image analysis using ImageJ (see SI, Section 2 for method) validated the reliability of the achieved size control, consistent with results from analytical centrifugation (Figure S2).

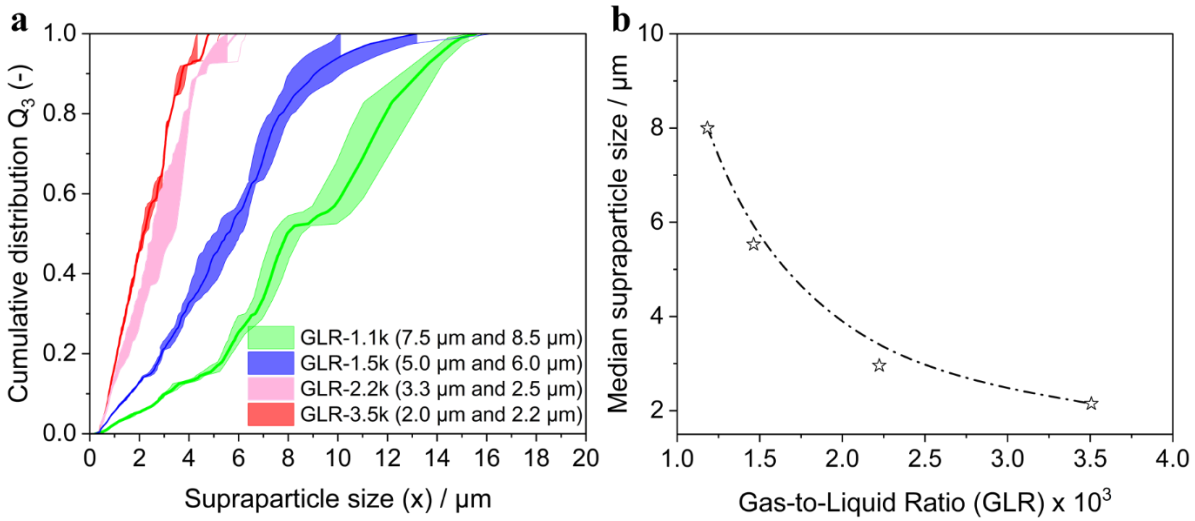

Figure 1. (a) Size distributions of supraparticles synthesized at varying GLRs (1.1k, 1.5k, 2.2k, and 3.5k) determined by analytical centrifugation. The distributions represent eight supraparticle powders with different median sizes (colored fields indicate the margin of deviation after repeated spray drying experiments). (b) Median supraparticle sizes (average of medians from two size distributions shown in Figure 1a) as a function of the GLR, with a dash-dotted line included as a visual guide.

In summary, we successfully produced supraparticles with both wide and narrow size distributions that enable us in the next step to systematically explore their effects on electrode processing and performance. We expect wide distributions to enhance packing and offer better connectivity at the electrode level. Narrow distributions enable control of the smoothness of the electrode surface and result in higher electrode porosities for improved electrolyte penetration. Specifically, these findings set the stage for further investigating the impact of the supraparticle size distribution on powder properties, slurry behavior, coating density, and electrochemical performance. As a note for the reader: the following discussion will use median sizes of 7.5, 5.0, 3.3, and 2.0 µm to represent the four supraparticle samples.

3.2. Morphology of supraparticle powders

The morphology of the supraparticle powders, with median sizes of 7.5, 5.0, 3.3, and 2.0 µm, was analyzed by SEM, as shown in Figure 2. Across all samples, supraparticles consist of agglomerated Si/C nanoparticles, forming micron-sized secondary particles.

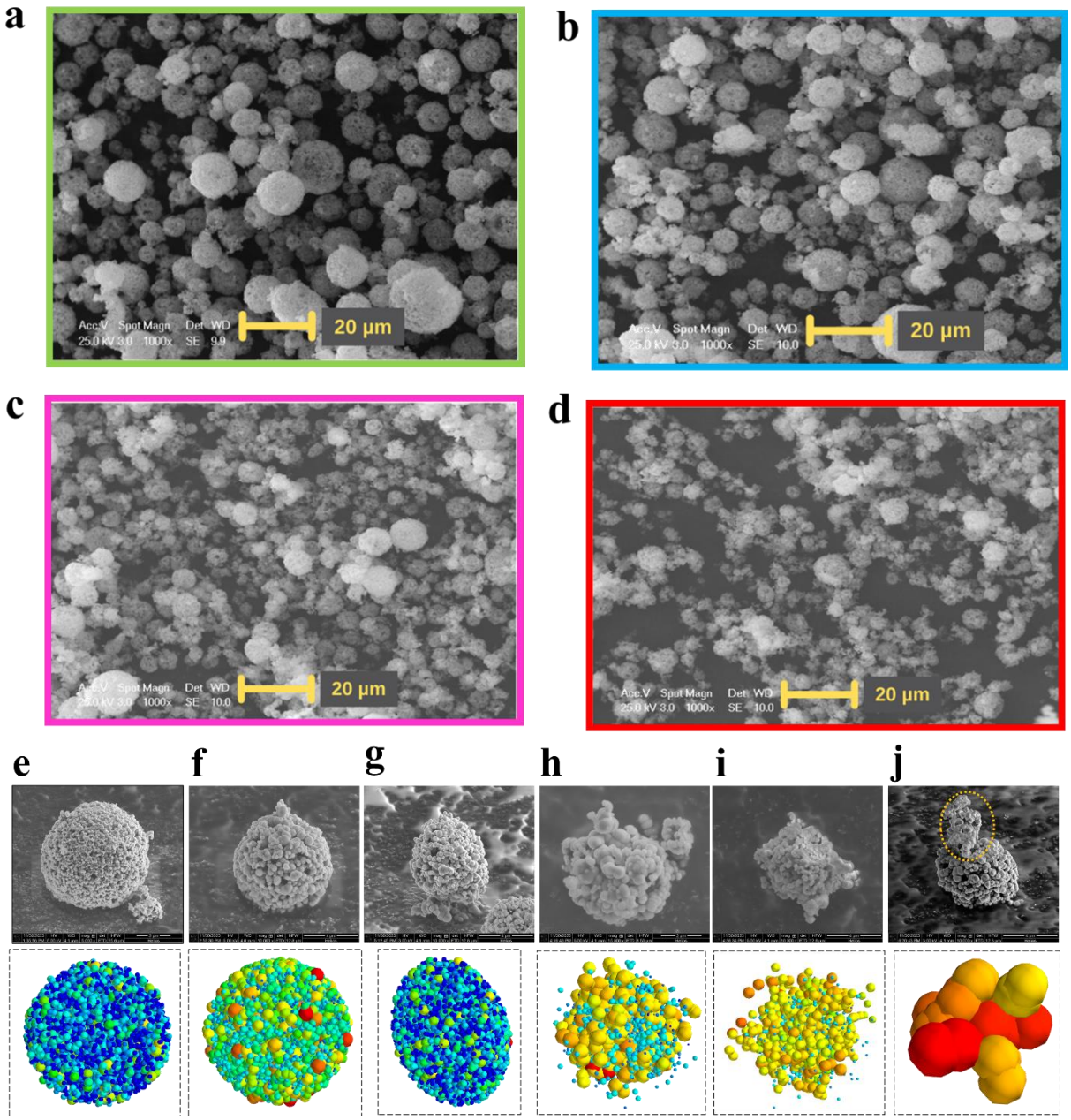

Figure 2. SEM images showing the morphology of the supraparticle powder samples of different median sizes used in this study: (a-d) supraparticle samples of median size 7.5, 5.0, 3.3, and 2.0 µm at 1000x magnification. SEM images and 3D-rendered schematics of individual supraparticles (schematics shown below each SEM image): (e, f) spherical with varying nanoparticle coverage; (g) ellipsoidal; (h) wavy surface morphology; (i) sub-rounded; (j) colloidal cluster-like.

The produced powders include a range of supraparticles, from smooth textured, spherical forms (referred to as multi-nanoparticle spherical supraparticles[25]) to wavy ones (nearly spherical supraparticles), ellipsoidal, subrounded, and colloidal cluster-like [26] supraparticles. In addition

to the SEM images, 3D-rendered schematics are provided in Figure 2e-j to conceptually illustrate the general structural features and shapes of the different types of supraparticles. These 3D schematics of supraparticles were simulated using a Python-based approach with the numpy, mayavi, and scipy libraries (for details, see characterization methods in SI, Section 2). While precise proportions of these forms are unavailable, visual observations offer valuable insights into their distribution.

In Figure 2a and 2b, supraparticles with median sizes of 7.5 µm and 5.0 µm predominantly exhibit smooth, spherical morphologies (see exemplary images in Figure 2e-f), with some larger particles in the 7.5 µm sample displaying hollow structures (Figure S3). These hollow forms arise from low particle concentration within a large droplet during spray drying, where larger droplets solidify into a thicker outer shell with a less dense interior. Such voids can promote non-uniform electrolyte penetration, leading to localized SEI growth. They further may reduce mechanical stability during battery cycling, potentially causing particle collapse or cracking.

For the smaller supraparticle powders, with median sizes of 3.3 µm and 2.0 µm, the particles tend to exhibit more irregular, wavy surface morphologies (Figure 2c and 2d, exemplary schematic image in Figure 2g-h) along with few spherical supraparticles. These irregularities are particularly pronounced in the 2.0 µm sample, where particles show sub-rounded or ellipsoidal shapes, contributing to higher surface roughness compared to the smoother, larger supraparticles. These irregular shapes may reduce packing efficiency and mechanical stability, resulting in less dense electrode layers.

The observed morphological variations across the different supraparticle sizes are critical because they influence the physical packing properties and electrochemical performance of the electrodes. In subsequent sections, we will explore how these morphological differences affect textural properties, coating quality and electrode performance metrics during cycling.

3.3. Effect of supraparticle size distribution on powder properties

3.3.1. Effect on textural properties

Textural properties of supraparticle powders were assessed using MIP and nitrogen adsorption, showing distinct porosity variations with particle size. Nanoparticle powders served as a reference. The mercury intrusion mechanism in supraparticle powders is shown in Schematic S1. Figure 3a shows differential pore diameter distributions for supraparticles with median sizes of 5.0, 3.3, and 2.0 µm. Macropore sizes in the 7.5 µm sample were estimated from cross-sectional images (Figure 3b), with an uncut supraparticle image in Figure S4.

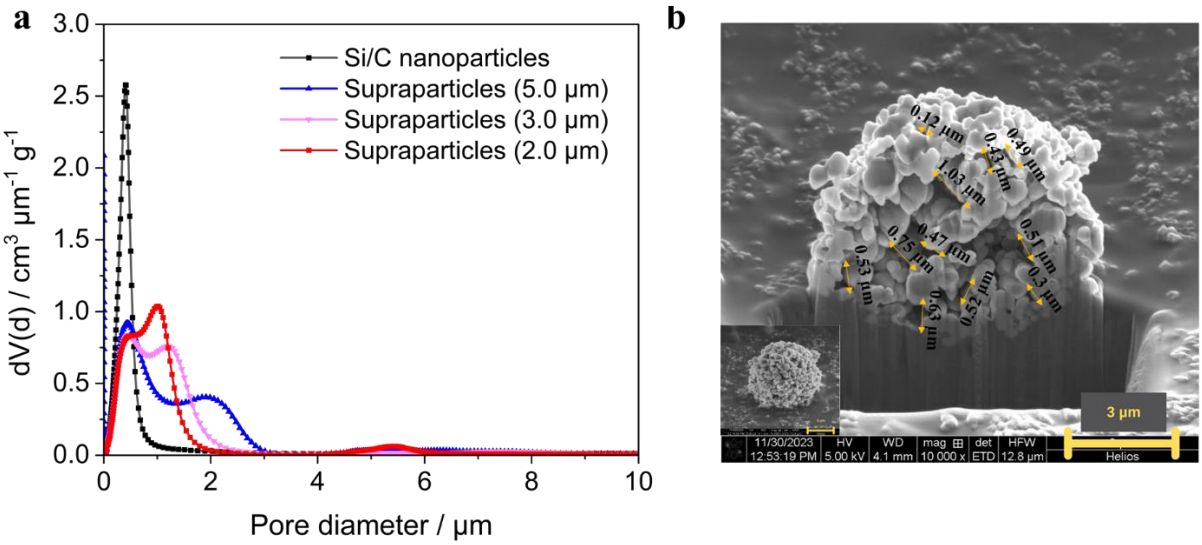

Figure 3. (a) Differential pore size distributions derived by MIP from powders of Si/C nanoparticles and their supraparticles (median sizes: 5.0, 3.3, and 2.0 µm). (b) Showcase FIB-SEM cross-sectional image illustrating pore sizes within the supraparticle structure of the 7.5 µm median-sized sample. The inset shows the intact supraparticle before the FIB-cut (image scale is same as FIB-cut image).

The nanoparticle powder exhibited a single sharp peak at a pore diameter of 0.41 µm, extending up to 2 µm. These pores originate from spacing between the non-porous nanoparticles due to imperfect packing. For the supraparticles, two types of porosity are considered: intraparticle porosity and interparticle porosity. Intraparticle porosity refers to the pores between primary nanoparticles within a single supraparticle, resulting from the hierarchical assembly during

spray drying. In contrast, interparticle porosity refers to the spacing between separate supraparticles, primarily influenced by the packing density in the powder.

Smaller supraparticles (2.0 µm and 3.3 µm) exhibited a bimodal pore size distribution, characterized by intraparticle macropores ranging from 0.1 to 0.85 µm and 0.1 to 0.62 µm, respectively. Their interparticle spacing extended from 0.85 to 2.4 µm and 0.62 to 2.1 µm. In contrast, medium-sized supraparticles (5.0 µm) showed fewer, but larger, interparticle spacing ranging from 1.2 to 3.0 µm, with intraparticle macropores peaking around 0.43 µm. Large supraparticles (median size 7.5 µm, Figure 1b) showed intraparticle macropores in the diameters range from 0.12-0.89 µm as can be seen from the SEM image cross section. The entire supraparticle is shown in the inset with same scale-bar as FIB-cut image.

Interestingly, the medium-sized supraparticle powder (5.0 µm) demonstrated the densest pore structure, with well-packed particles achieving a balance between intraparticle macropores and interparticle spacing. Their wide supraparticle size distribution allowed smaller particles to fill spacing between larger ones, leading to a cumulative mercury intrusion specific volume (Figure S5) of 1.75 $cm^3\ g^{-1}$, which is lower than that of the 3.3 µm (1.85 $cm^3\ g^{-1}$) and 2.0 µm (2.0 $cm^3\ g^{-1}$) samples, but still higher than the intruded volume of the nanoparticle-sized powder (1.38 $cm^3\ g^{-1}$). These findings suggest that optimizing not only the supraparticle median diameter but the supraparticle size distribution is critical for improving electrode layer porosity and mechanical stability. Moreover, mercury intrusion results indicate that powders with smaller, non-spherical supraparticles (2.0 µm) exhibited larger intrusion volumes and higher overall porosity, which could negatively impact the structural integrity of the anode layer. The larger content of pore surfaces may facilitate excessive SEI formation, leading to performance degradation over time.

These results highlight the delicate interplay between supraparticle size and textural properties, which may affect electrode performance, setting the stage for further analysis of slurry behavior and coating quality in the following sections.

3.3.2. BET and SEI specific area

Brunauer–Emmett–Teller (BET) surface area analysis provided insights into the specific surface area of the supraparticle powders. Respective analyses (Figure S6) showed that all supraparticle powders exhibited a similar specific surface area (SSA) with an average value of 5.36 ± 0.09 m^2g^{-1}, as expected from adsorption-based measurements. Notably, the SSA of the supraparticles is ~ 28.5 % lower than that of the Si/C composite nanoparticles, which have a significantly higher surface area due to their lower degree of agglomeration and thus a higher degree of surface exposure.

Despite the consistent SSA across supraparticle sizes, their lower surface area compared to Si/C nanoparticles helps limit the SEI formation. Higher surface areas, like those of the Si/C nanoparticles, tend to promote more extensive SEI growth, leading to greater initial lithium consumption. Preliminary results (BET) already suggest that the lower SSA of supraparticles is expected to reduce SEI growth, potentially improving cycling stability and offering better long-term performance.

We hypothesize that the supraparticles, as secondary structures, can confine significant SEI formation to their outer surfaces (exposed to neighboring supraparticles) compared to inner ones, a phenomenon observed in similar secondary structures by other researchers.[27,28] A peripheral-limited SEI formation is expected to result in even lower specific volume of SEI depending on the surface-to-volume ratio of the particles.

3.4. Effect of supraparticle size distribution on processability and coating characteristics

3.4.1. Effect on slurry rheology

The rheological behavior of slurries plays a key role in determining the uniformity and performance of electrode coatings.[29,30] Figure 4a and 4b depicts shear-dependent and time-dependent (three interval thixotropy test, 3iTT test [31]) rheological characteristics of the slurries made from supraparticles of varying sizes (7.5, 5.0, 3.3, and 2.0 µm), alongside a reference slurry made from pristine Si/C composite nanoparticles. The findings reveal distinct differences in viscosity and shear recovery, suggesting that supraparticles offer significant advantages in enhancing slurry handling and coating stability.

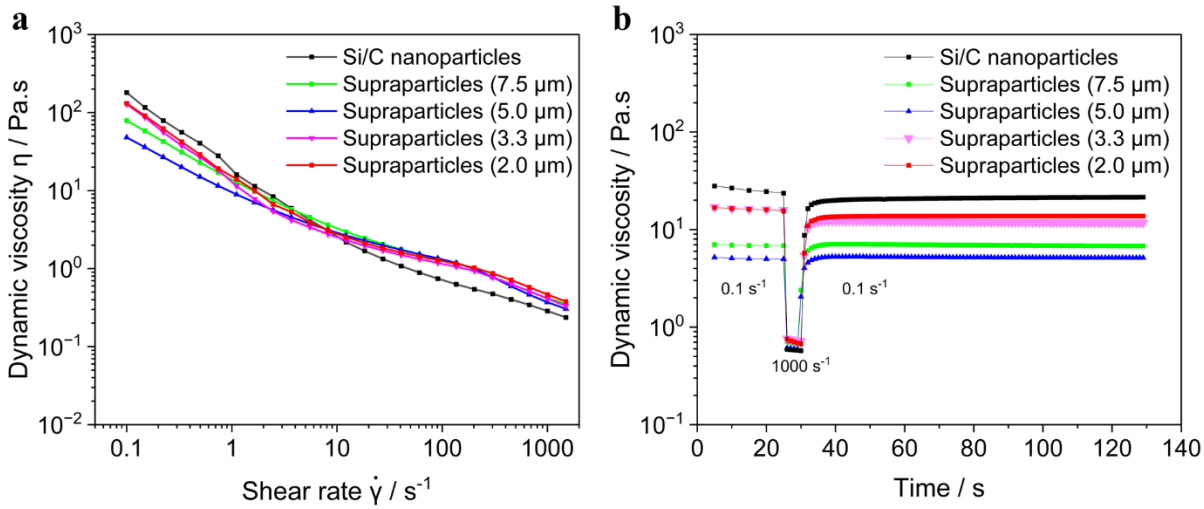

Figure 4. (a) Steady state dynamic viscosity-shear rate curves. (b) Time-dependent rheological characteristics (three interval thixotropy test, 3iTT) of slurry samples made from Si/C composite nanoparticles and supraparticles with median sizes of 7.5, 5.0, 3.3, 2.0 µm. Data points were taken in unsteady state mode. Cone-plate geometry of cone angle 1° was used. The measurement temperature was set at 20 °C.

At low shear rates (0.1 s^{-1}), the nanoparticle-based slurry exhibits a significantly higher viscosity (182.5 Pa·s) compared to the supraparticle-based slurries (7.5, 5.0, 3.3, and 2.0 µm) with viscosity values of 80, 47, 124 and 130 Pa·s, respectively. This indicates that nanoparticle slurries form stronger structures due to stronger intermolecular interactions between smaller particles in the slurry. According to Woodcock's equation,[32] smaller particles reduce inter-

particle distances, facilitating aggregation. This increases the effective solid volume fraction, leading to a highly viscous slurry. As the shear rate increases, the viscosity of all slurries decreases which is a typical characteristic of shear thinning fluids.[33] Interestingly, at higher shear rates (beyond 100 s^{-1}), the viscosities of all slurries converge and exhibit similar flow properties during processing at application shear of 1000 s^{-1} (calculated as the ratio of the line speed – the speed at which the doctor blade moves across the static substrate – and the blade gap – the vertical distance between the doctor blade and the substrate[34]).

Although the viscosities are similar at high shear rates, the differences in behavior become apparent once the shear is removed (thixotropic structure recovery), as shown in Figure 4b. Table S1 lists the reference viscosity and the recovered viscosity values for each sample, measured 20 seconds after the shear rate was removed. Supraparticles with medium and larger sizes (5.0 µm and 7.5 µm) show full structural recovery within 20 seconds, whereas smaller supraparticles and nanoparticles only partially recover (70-80 %). This faster recovery in larger supraparticles hints at their potential for stabilizing the slurry structure during coating, an important factor for ensuring uniform layer formation.

These porosity-driven viscosity differences, combined with particle morphology (size, shape, internal structure, surface texture), strongly influence the viscoelastic properties of the slurries, such as their ability to recover structure after the shear rate was removed (as demonstrated by 3iTT tests in Figure 4b). For example, slurries with 5.0 µm supraparticles recover ~100 % of their initial viscosity within 20 seconds, compared to ~70-80 % recovery for small supraparticles (2.0 µm and 3.3 µm). The slow recovery of smaller supraparticle slurries induces shear-history effects, which can compromise process consistency. Altogether, these findings highlight the importance of optimizing interparticle porosity by precisely controlling spray drying parameters—such as solids concentration in the feed dispersion, droplet size, and drying temperature—to achieve favorable viscoelastic properties (e.g., balanced elasticity and

viscosity for consistent recovery), smooth slurry flow, reduced shear-history effects, and homogenous electrode coatings. The next section will explore how these rheological properties impact coating density and electrochemical performance, comparing the behavior of larger, medium and smaller supraparticles during testing and cycling.

3.4.2. Effect on stability against stress during processing and interface with current collector

High shear stresses during slurry mixing and coating can impact supraparticle integrity, potentially leading to breakage. To evaluate the structural integrity and the influence of supraparticle size on surface topography, AFM was used to visually examine the coated layers and calculate root mean square (RMS) roughness. RMS roughness, which reflects the standard deviation of surface heights, provides insights into surface texture and stability under stress.[35] Further, this roughness is important as it affects the interface between the coated layer and the current collector.

Figure 5 presents surface topography images (a-d, left panel), RMS roughness values (e, right panel), and roughness profiles (f, bottom) for electrodes made from various supraparticle size distributions. For comparison, the RMS value and roughness profile of the nanoparticle-based coatings are also shown in grey (right panel in a bar graph and left-bottom as line profile).

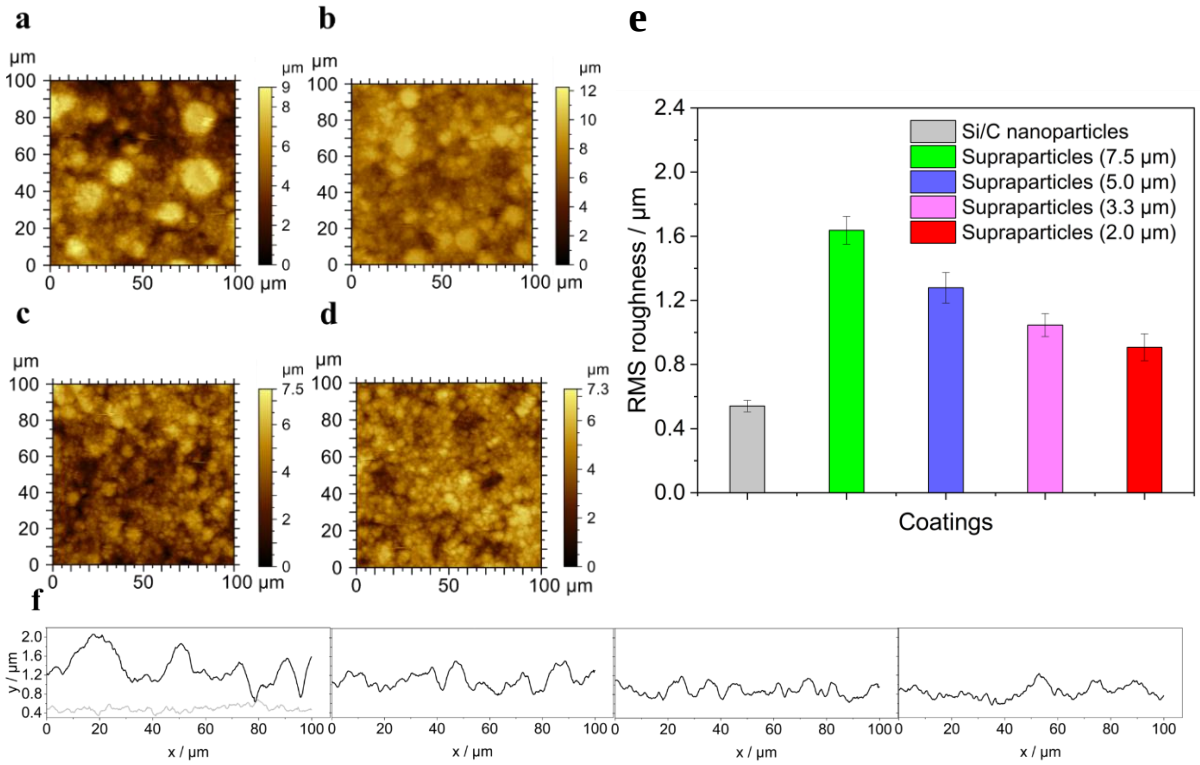

Figure 5. Contact mode AFM topography of coatings. From (a-d) Si/C composite supraparticles with different median sizes of 7.5, 5.0, 3.3, and 2.0 µm, respectively. (e) Average values of RMS roughness (µm) for the corresponding coated layers. (f) Bottom: corresponding horizontal topography profiles of the 100 x 100 µm² area of the coated samples. The topography profile of Si/C nanoparticles is shown as reference in grey color.

The 2D AFM surface topography images (Figure 5, panels a-d) demonstrate the presence of supraparticles within the coatings, indicating their mechanical stability during the slurry preparation and coating process. The average RMS roughness values (Figure 5e) increase with (supra)particle size, from 0.54 µm ± 0.03 µm for nanoparticle-based layers to significantly rougher surfaces for the large supraparticles (up to 1.63 µm ± 0.08 µm).

All supraparticles, regardless of size, form a pseudo-point contact interface with the copper current collector. While the contact points are not perfectly sharp due to the copper's surface roughness (RMS roughness: 0.34 µm ± 0.05, Figure S7a-b), the wavy texture promotes effective interlocking at these points. These pseudo-point contacts create voids that can be filled with adhesive and conductive material, potentially enhancing adhesion and maintaining electrical pathways despite the roughness. Exemplary FIB-cut SEM images (Figure S8a-b)

show the interlocking between the supraparticle-based coated layers (with median particle sizes of 5.0 and 3.3 µm) and the current collector, highlighting the presence of voids. These voids, filled with softer materials, are similarly observed across the electrode surfaces of all four supraparticle-based coatings (Figure S9a-j).

Nanoparticles also demonstrate good interlocking with the copper foil as their roughness closely matches that of the copper surface. However, this results in fewer void spaces at the interface with the current collector to be filled with binder or conductive material (here: C65). Adhesion testing results (Figure S11) confirm that both nanoparticles and supraparticles of all sizes provide overall strong adhesion to the copper substrate, but the layers break cohesively during testing. This indicates that the failure occurs majorly within the coating itself rather than at the copper interface (details in SI, Section 3.11). However, during electrochemical testing, where electrodes are immersed in electrolyte and experience multidirectional stresses due to volume expansion and contraction, some degree of layer delamination from the copper surface may be observed after long term cycling.

These observations, along with the adhesion results (Figure S10), highlight that both nanoparticle-based and supraparticle-based coatings exhibit good adhesion to the substrate. However, differences in coating surface roughness, supraparticle sizes distribution, shape, slurry rheology and porosity, as observed in the mercury intrusion results, can influence the overall mechanical stability (see detailed reasoning of different failure modes in SI, Section 3.11) and performance of the electrode layers during cycling. Additionally, the spacing at the interface between supraparticle-based layers and the copper surface may help mitigate the effects of silicon's volume expansion and contraction during cycling, as these stresses are distributed in both directions. Larger voids associated with larger supraparticles are expected to scale similarly to the surface roughness, potentially contributing to better stress accommodation and improved long-term stability.

3.4.3. Effect of supraparticle size distribution on the density of coated layers

Achieving high packing density in electrode layers is important, especially for applications where space and weight are constrained, such as electric vehicles and portable electronics. Supraparticle structuring offers a strategic advantage by enabling more efficient packing[13] and better thickness control compared to the direct usage of nanoparticles in coatings, which often suffer from uneven thickness and uncontrolled porosity.[36]

Figure 6 presents the mass densities of coatings produced from Si/C composite supraparticles with median supraparticle sizes of 7.5, 5.0, 3.3, and 2.0 µm. The average coating mass densities (calculated from a total of 32 circular-shaped electrodes) for these sizes are 0.83, 0.90, 0.80, and 0.77 g cm^{-3}, respectively. The highest average coating mass density, 0.90 g cm^{-3}, was achieved using supraparticles with a median diameter of 5.0 µm, while the lowest coating density (0.77 g cm^{-3}) was observed for the 2.0 µm-sized supraparticles. This shows that medium-sized supraparticles tend to result in a more densely packed coating compared to smaller or larger particles as also expected from MIP results.

Compared to reference coatings made from Si/C nanoparticles (0.73 g cm^{-3}), supraparticles show a 6.5–23% increase in density. This improvement is attributed to two key factors: their low yield stress, which ensures thinner layers, and their fast thixotropic recovery, which promotes layer homogeneity. The rapid structural recovery of supraparticles allows them to stabilize their packing structure quickly during drying. Additionally, the pre-aggregated clusters of nanoparticles in supraparticles act as large units that resist local particle aggregation, settling into compact and stable positions immediately after the shear stress is removed. Their low yield stress (0.1–3.0 Pa) facilitates sufficient shrinkage during drying, minimizing void formation and resulting in uniform, thinner layers.

In contrast, the increased thickness and inconsistency observed in nanoparticle-based coatings are attributed to their reduced shrinkage ability during drying and local aggregation, further

amplified by their slower structural recovery. The high yield stress (~ 15.5 Pa) of nanoparticle slurry limits significant shrinkage as the solvent evaporates, leading to thicker layers. Additionally, the high surface energy of nanoparticles promotes local aggregation, which contributes to inconsistent porosity within the coating. This then finally appears as inconsistent thickness throughout the coating.

The decrease in coating density for smaller supraparticles (2.0 µm and 3.3 µm) is attributed to their narrower size distributions and varied shapes (rounded, sub-rounded, and colloidal cluster-like), which make efficient packing more difficult. On the other hand, while the 7.5 µm supraparticles show a slightly lower density than the 5.0 µm ones, this can be explained by the presence of some hollow supraparticles (Figure S3) and fewer small particles (Figure 1a) to fill the gaps between larger ones, leading to a less compact structure.

While the mass densities of supraparticle-based coatings (0.77–0.90 g cm^{-3}) are promising, they fall short of the theoretical density (2.02 g cm^{-3}) for the Si/C, C65, and PAA mixture due to voids and porosity. Smaller supraparticles (2.0 µm) create more interparticle spacing, while 5.0 µm supraparticles achieve better packing efficiency. Optimizing size distribution, slurry formulation, or calendering could help close this gap while maintaining a crucial balance between porosity and tortuosity, ultimately enhancing both packing density and performance.

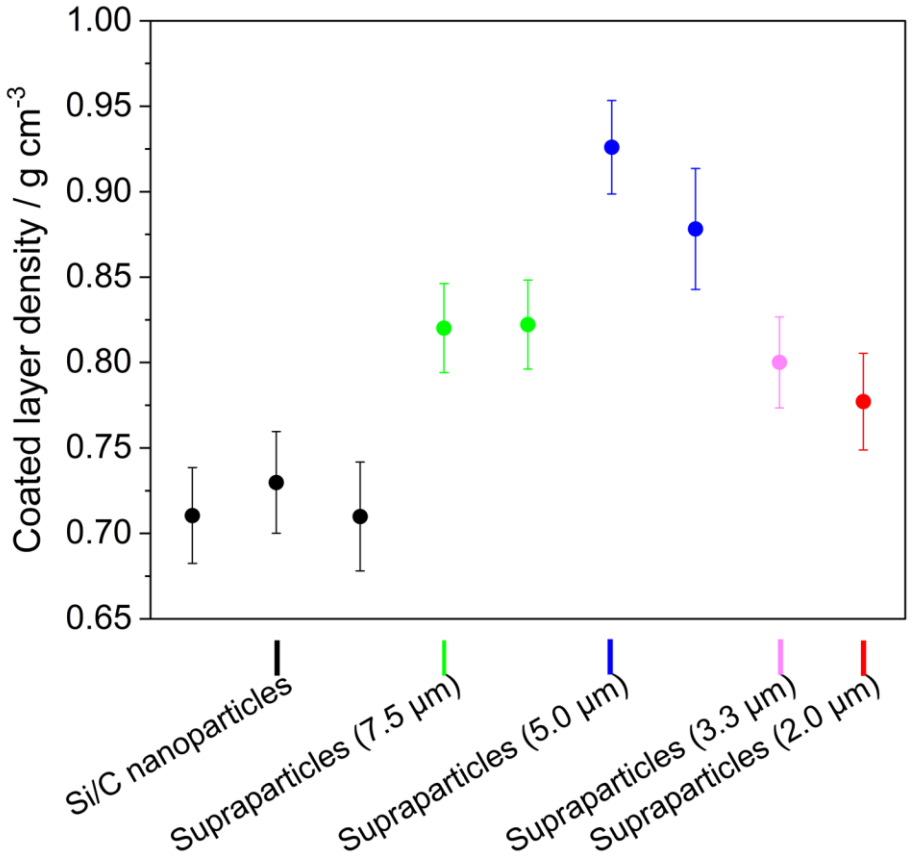

Figure 6. Mass densities of coatings produced from Si/C composite supraparticles with median sizes of 7.5 µm (green), 5.0 µm (blue), 3.3 µm (magenta), and 2.0 µm (red), with Si/C composite nanoparticle-based coatings (black) included as a reference. All slurries had a total solid mass fraction of 0.4. Each dot represents the average coating density from 32 electrodes, with error bars indicating the standard deviation.

3.5. Effect of supraparticle size distribution on electrochemical performance

Finally, the electrochemical performance of the supraparticles with different size distributions was analyzed. The capacity calculations for the lithium half-cell are based on the overall weight of the Si/C active material. CE and capacity retention values represent the average of two electrodes in both the main and supplementary data, unless otherwise specified.

3.5.1. Coulombic efficiencies

The CE progression for supraparticles of different sizes reveals interesting trends across cycles. As shown in Figure 7a, the first-cycle CEs for electrodes made from supraparticles with median sizes of 7.5, 5.0, 3.3 and 2.0 µm, follow a clear decreasing trend from large to small sizes, with CEs of 87.9, 87.5, 86.5 and 84.9 %, respectively. Electrodes made from nanoparticles, by

comparison, exhibit much lower first-cycle CE (65 %) as reported before[13] due to more extensive SEI formation and uncontrolled porosity.

The larger and medium-sized supraparticles (7.5 µm and 5.0 µm) demonstrate higher first-cycle CEs, most probably due to reduced SEI formation, aligning with the hypothesis presented earlier (Section 3.2.2) that a lower SSA reduces SEI growth, thus improving CE.

Despite the similar BET SSA across all supraparticle sizes, we attribute the slight difference in first-cycle CEs between the largest and smallest supraparticles of around 3 % to the impact of porosity. Since the SEI forms not only on the outer surfaces of the supraparticles but also within pore spaces, the majority of SEI is confined to the outer surfaces, with much less SEI forming internally within the supraparticles. This variation is closely tied to the differences in interparticle and intraparticle pores. Mercury intrusion data for supraparticles of different sizes (5.0, 3.3, and 2.0 µm) revealed total mercury intrusion specific volumes of 1.75, 1.85, and 2.0 $cm^3\ g^{-1}$, respectively—volumes that inversely correlate with the observed CEs.

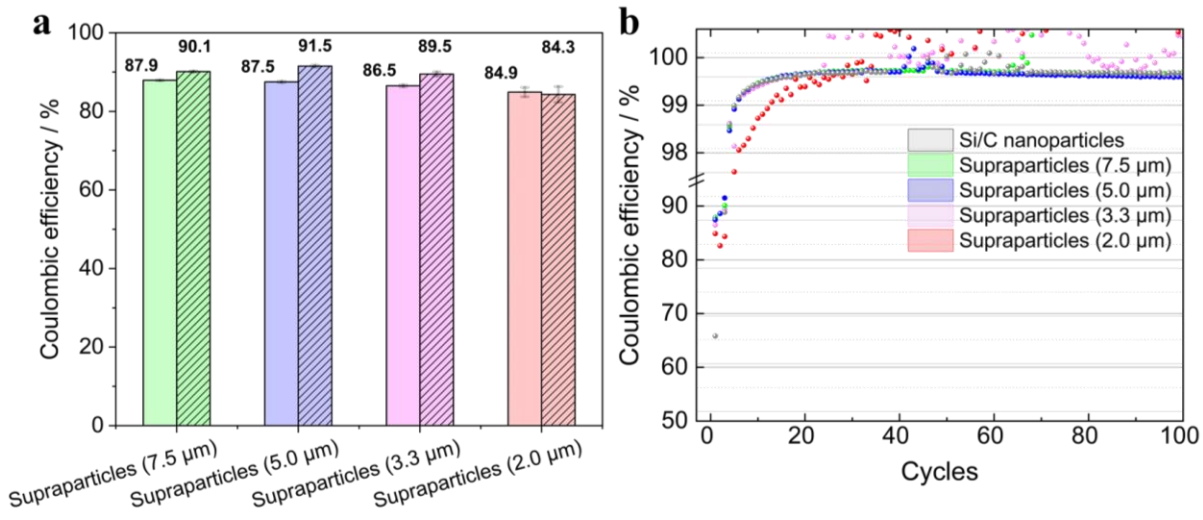

Figure 7. CEs of electrodes made from supraparticle powders with different median sizes of 7.5 µm (green), 5.0 µm (blue), 3.3 µm (magenta) and 2.0 µm (red): a) bar graphs showing the 1st and 3rd cycle CEs, and (b) progression of the CE (dots) over 100 cycles for these supraparticle sizes and nanoparticles-based reference coatings. CEs > 100 %, though being nonphysical were kept as they indicate degradation, for example by fracture in the anode due to volume expansion that brings trapped Li^+ from previous cycles back into system. CEs of electrodes from Si/C nanoparticles[13] are shown as reference.

The implications are clear: smaller supraparticles with higher pore spacing facilitate more SEI formation, leading to lower first-cycle CE. In contrast, larger supraparticles, particularly those with wider supraparticle size distributions, exhibit reduced pore spacings, which reduces the SEI growth and boosts the overall formation cycles CEs. These findings highlight the intricate relationship between surface area, porosity, and CE performance which is controlled by not only the particle size distribution but also slurry rheological properties.

From the 3rd cycle onward (at 0.5 C), medium-sized supraparticles (5.0 µm) consistently outperform both smaller and larger supraparticles in maintaining the highest and stable CE (Figure 7b), suggesting an optimal balance between surface area, porosity, and structural integrity. This stability, extending up to 100 cycles, further hints at the importance of

supraparticle size distribution for long-term performance, particularly as smaller supraparticles (2.0 and 3.3 µm) show significant fluctuations in CE starting from the 25th cycle. These fluctuations signal potential structural degradation or SEI reformation, pointing to the need for further optimization of supraparticle size and size distribution for enhanced cycling stability.

3.5.3. Cycling stability

Figure 8 shows the cycling performance of supraparticles with different median sizes and size distributions. The Si/C composite nanoparticles curve, as reported previously by us, is used as a reference for discussion.[13]

It becomes clear that the cycling performance of electrodes made from supraparticles, and nanoparticles shows significant differences, depending on their median size and size distribution. For supraparticles with median sizes of 2.0, 3.3, 5.0, and 7.5 µm, capacity retention (reference to 3rd cycle) after 50 cycles was 81, 88.9, 90.6, and 86.7 %, respectively. After 100 cycles, retention dropped to 69.7, 81.9, 86.2, and 81.5 %, respectively.

The better cycling stability of medium-sized supraparticles (5.0 µm) suggests an optimal balance between structural integrity and efficient Li-ion transport. These supraparticles exhibited fewer capacity fluctuations and better resistance to stress-induced degradation compared to smaller and larger particles. The performance gains with medium-sized supraparticles are attributed to their structural stability, reduced SSA (compared to nanoparticles), and optimized pore space, which together mitigate the effects of volume expansion and enhance long-term stability.

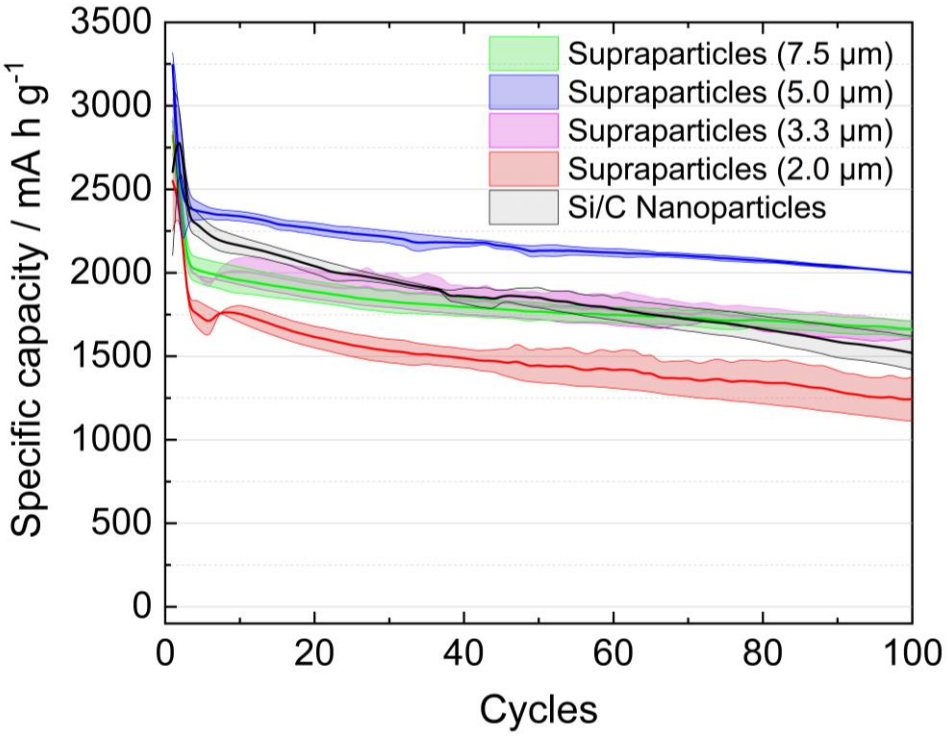

Figure 8. Specific delithiation capacity (represented by lines) for supraparticles with varying size distributions, denoted by red, magenta, blue and green lines corresponding to median particle sizes of 2.0, 3.3, 5.0, and 7.5 µm, respectively. The cycling curve of the Si/C composite nanoparticles (dark) was previously published by us.[13] It is reprinted and used as a reference for discussion under the terms of the CAA 4.0 License (CC BY, http://creativecommons.org/licenses/by/4.0/).

Interestingly, both large (7.5 µm) and small (3.3 µm) supraparticles exhibited similar capacity retention up to the 180th cycle. However, from the 180th cycle onwards, larger supraparticles demonstrated better retention (69 % *vs.* 64.4 % for the 3.3 µm particles) with a discharge capacity of 1409 mAh g^{-1} at the 202nd cycle (Figure S11). This suggests that larger supraparticles offer enhanced stability in prolonged cycling compared to their smaller counterparts. In contrast, Si/C nanoparticles show capacity retentions like small supraparticles (3.3 µm) up to 100 cycles but on average nanoparticles-based electrodes clearly degrade faster (Figure S11). This difference is attributed to the higher SSA of nanoparticles, which increases

their available surface for SEI formation, combined with larger pore spacing that further exacerbates volume expansion effects. Collectively, these induce greater stress and accelerate structural degradation, ultimately resulting in contact loss with carbon agents or the current collector during cycling.

Finally, our findings align closely with the mechanical-electrochemical simulation results from Wu and Lu, who analyzed agglomerates in Li-ion batteries.[37] Their simulations evaluated stress distribution within secondary particles (supraparticles) of different sizes during cycling. The results revealed that larger supraparticles are more effective at mitigating stress compared to smaller ones, underscoring the critical role that the secondary particle size plays in managing mechanical stress within lithium-ion battery electrodes. This highlights the importance of optimizing supraparticle size to enhance both cycling stability and overall electrode performance.

3.6. Importance of size control and sensitivity

Figure S15 shows the cycling performance of supraparticles with sizes between and exceeding those in Figure 8, which have not been discussed previously. Analyzing Figures 8 and S12 reveals that electrodes made of supraparticles (≥ 5.0 µm) exhibit consistent and reproducible performance. For comparison, data from smaller supraparticles (e.g., 2.5 µm size in Figure S12), which have not been discussed previously, show a significant capacity drop in the first few cycles due to electrical isolation caused by volume expansion. Accordingly, adhesion analysis (Figure S10) points towards a cohesive failure in smaller supraparticles. It is important to note that as the median size of the supraparticles increases to 8.5 µm (Figure S12), the rise of CEs in later cycles slows down. This is likely due to increased internal porosity, as also observed for 7.5 µm supraparticles, which acts as an additional degradation mechanism for electrodes made from very large supraparticles influenced by process conditions, such as particle mass loading in the spray-dying-dispersion and the chosen spray drying parameters.

Conclusion

This study investigates the impact of sizes (associated morphologies) and size distributions of supraparticles on slurry behavior, coating quality, and electrochemical performance in Li-ion batteries. Structuring nanoparticles into supraparticles presents a significant advantage, offering improved handling, reduced SEI formation, and enhanced electrochemical performance. Our findings are summarized as follows:

Supraparticle Morphology and Connectivity: Larger (7.5 µm) and medium-sized (5.0 µm) supraparticles exhibit better packing efficiency, providing well-defined ion transport pathways and improved electrical connectivity. Anodes made of smaller supraparticles (2.0 µm and 3.3 µm) exhibit higher porosity, leading to less uniform packing and lower performance.

Rheology and Coating Density: Larger and medium sized supraparticles exhibit better thixotropic recovery, leading to more uniform coatings with higher density compared to nanoparticle-based coatings and coatings made of smaller supraparticles. This contributes to enhanced electrode stability and performance.

SEI Formation: Supraparticles confine SEI formation mostly to their outer surfaces (surfaces exposed to interparticle pores/spacing around supraparticles), minimizing internal SEI due to their compact structure, which retains internal macropore space for silicon expansion. Larger supraparticles with wide size distributions and smaller surface-to-volume ratios reduce the pore volume in the layers and provide smooth surfaces, thereby promoting stable SEI formation, improving CE, and enhancing cycle stability.

Cycling Performance: Medium-sized supraparticles (5.0 µm) provide an optimal balance of initial capacity, CE, and cycle retention, outperforming both smaller and larger particles in long-term stability. However, it's important to note that the increased internal porosity and hollow structures within large supraparticles introduce an additional degradation mechanism for their electrodes, influenced by process factors such as particle mass loading and spray-

drying parameters. Therefore, developing larger yet denser supraparticles is anticipated to enhance performance. Optimizing supraparticle size distribution and density is crucial for controlling porosity and stability, improving cycling performance. In this context, intraparticle macropores are as crucial as interparticle spacing, as altering the size of the initial building blocks significantly affects their balance.

Recommendation: From insights gained from the overall results in this study we recommend medium sized supraparticles of sizes range 5-6.5 µm with average around 6.0 µm as the optimum sizes of supraparticles for high-energy applications.

Future Applications: The control over porosity and particle distribution demonstrated in this study suggests that further optimization could significantly enhance not only battery performance but also other applications requiring high porosity control, such as fuel cells and electrolyzers. Therefore, the insights gained from this study extend beyond improving layer uniformity, demonstrating that controlling layer porosity using supraparticles is both feasible and effective, as evidenced by mercury intrusion results. Both interparticle pores/spacing, dictated by supraparticle size and shape, and intraparticle pores, influenced by nanoparticle size, play critical roles in optimizing performance.

Conflict of interest

All authors have approved the submission and have no conflicts of interest to disclose.

Acknowledgements

The authors gratefully acknowledge financial support from the Federal Ministry of Economic Affairs and Climate Action, Germany (Funding code 03EI3027A). Additionally, we appreciate the support from the Interdisciplinary Center for Analytics on the Nanoscale (ICAN) at the University of Duisburg-Essen (DFG RIsources reference: RI_00313), a DFG-registered core facility (Project Nos. 233512597 and 324659309), for TEM, SEM, and FIB-SEM

measurements. We also thank the Open Access Publication Fund of the University of Duisburg-Essen for their support.

References

(1) Kräenbring, M.-A.; Wickert, L.; Hansen, M.; Sanden, S.; Pellumbi, K.; Wolf, J.; Siegmund, D.; Özcan, F.; Apfel, U.-P.; Segets, D. Navigating through Complexity: Optimizing Cathodes for Organic Electrohydrogenation through Coherent Workflows. *ChemCatChem* **2024**, *16* (3). DOI: 10.1002/cctc.202301273.

(2) Kim, U.-H.; Lee, S.-B.; Park, N.-Y.; Kim, S. J.; Yoon, C. S.; Sun, Y.-K. High-Energy-Density Li-Ion Battery Reaching Full Charge in 12 min. *ACS Energy Lett.* **2022**, *7* (11), 3880–3888. DOI: 10.1021/acsenergylett.2c02032.

(3) Bitew, Z.; Tesemma, M.; Beyene, Y.; Amare, M. Nano-structured silicon and silicon based composites as anode materials for lithium ion batteries: recent progress and perspectives. *Sustainable Energy Fuels* **2022**, *6* (4), 1014–1050. DOI: 10.1039/D1SE01494C.

(4) Eftekhari, A. Lithium Batteries for Electric Vehicles: From Economy to Research Strategy. *ACS Sustainable Chem. Eng.* **2019**, *7* (6), 5602–5613. DOI: 10.1021/acssuschemeng.8b01494.

(5) Lu, L.; Han, X.; Li, J.; Hua, J.; Ouyang, M. A review on the key issues for lithium-ion battery management in electric vehicles. *Journal of Power Sources* **2013**, *226*, 272–288. DOI: 10.1016/j.jpowsour.2012.10.060.

(6) Zhang, C.; Wang, F.; Han, J.; Bai, S.; Tan, J.; Liu, J.; Li, F. Challenges and Recent Progress on Silicon-Based Anode Materials for Next-Generation Lithium-Ion Batteries. *Small Structures* **2021**, *2* (6). DOI: 10.1002/sstr.202100009.

(7) Salah, M.; Murphy, P.; Hall, C.; Francis, C.; Kerr, R.; Fabretto, M. Pure silicon thin-film anodes for lithium-ion batteries: A review. *Journal of Power Sources* **2019**, *414*, 48–67. DOI: 10.1016/j.jpowsour.2018.12.068.

(8) Liu, Q.; Meng, T.; Le Yu; Guo, S.; Hu, Y.; Liu, Z.; Hu, X. Interface Engineering to Boost Thermal Safety of Microsized Silicon Anodes in Lithium-Ion Batteries. *Small methods* **2022**, *6* (7), e2200380. DOI: 10.1002/smtd.202200380. Published Online: Jun. 1, 2022.

(9) Le Cao, K. A.; Ogi, T. Advanced carbon sphere-based hybrid materials produced by innovative aerosol process for high-efficiency rechargeable batteries. *Energy Storage Materials* **2025**, *74*, 103901. DOI: 10.1016/j.ensm.2024.103901.

(10) Orthner, H.; Wiggers, H.; Loewenich, M.; Kilian, S.; Bade, S.; Lyubina, J. Direct gas phase synthesis of amorphous Si/C nanoparticles as anode material for lithium ion battery. *Journal of Alloys and Compounds* **2021**, *870*, 159315. DOI: 10.1016/j.jallcom.2021.159315.

(11) Zhao, M.; Zhang, J.; Wang, W.; Zhang, Q. The preparation of mass producible, highly-cycling stable Si/C anode materials with nano-sized silicon crystals embedded in highly amorphous silicon matrix. *Nanotechnology* **2021**, *32* (48). DOI: 10.1088/1361-6528/ac2018. Published Online: Sep. 7, 2021.

(12) An, S. J.; Li, J.; Daniel, C.; Mohanty, D.; Nagpure, S.; Wood, D. L. The state of understanding of the lithium-ion-battery graphite solid electrolyte interphase (SEI) and its relationship to formation cycling. *Carbon* **2016**, *105*, 52–76. DOI: 10.1016/j.carbon.2016.04.008.

(13) Amin, A.; Loewenich, M.; Kilian, S. O.; Wassmer, T.; Bade, S.; Lyubina, J.; Wiggers, H.; Özcan, F.; Segets, D. One-Step Non-Reactive Spray Drying Approach to Produce Silicon/Carbon Composite-Based Hierarchically Structured Supraparticles for Lithium-Ion Battery Anodes. *J. Electrochem. Soc.* **2023**, *170* (2), 20523. DOI: 10.1149/1945-7111/acb66b.

(14) Amin, A.; Bade, S.; Kilian, S. O.; Loewenich, M.; Lyubina, J.; Segets, D.; Wassmer, T.; Wiggers, H.; Özcan, F. Hierarchically structured Si/C agglomerates made by spray drying. WO2023/147853 A1.

(15) Cheng, X.; Tang, C.; Yan, C.; Du, J.; Chen, A.; Liu, X.; Jewell, L.; Zhang, Q. Preparation of porous carbon spheres and their application as anode materials for lithium-ion batteries: A review. *Materials Today Nano* **2023**, *22*, 100321. DOI: 10.1016/j.mtnano.2023.100321.

(16) Le Cao, K. A.; Iskandar, F.; Tanabe, E.; Ogi, T. Recent Advances in the Fabrication and Functionalization of Nanostructured Carbon Spheres for Energy Storage Applications. *KONA* **2023**, *40* (0), 197–218. DOI: 10.14356/kona.2023016.

(17) Andersen, H. F.; Foss, C. E. L.; Voje, J.; Tronstad, R.; Mokkelbost, T.; Vullum, P. E.; Ulvestad, A.; Kirkengen, M.; Mæhlen, J. P. Silicon-Carbon composite anodes from industrial battery grade silicon. *Scientific reports* **2019**, *9* (1), 14814. DOI: 10.1038/s41598-019-51324-4. Published Online: Oct. 15, 2019.

(18) Loewenich, M.; Orthner, H.; Wollny, P.; Wlokas, I.; Bade, S.; Lyubina, J.; Wiggers, H. Synthesis and upscaling of silicon nanoparticles for lithium-ion batteries in a hot-wall reactor. *Journal of Alloys and Compounds* **2024**, *986*, 174061. DOI: 10.1016/j.jallcom.2024.174061.

(19) McDowell, M. T.; Lee, S. W.; Harris, J. T.; Korgel, B. A.; Wang, C.; Nix, W. D.; Cui, Y. In situ TEM of two-phase lithiation of amorphous silicon nanospheres. *Nano letters* **2013**, *13* (2), 758–764. DOI: 10.1021/nl3044508. Published Online: Jan. 17, 2013.

(20) Wood, D. L.; Quass, J. D.; Li, J.; Ahmed, S.; Ventola, D.; Daniel, C. Technical and economic analysis of solvent-based lithium-ion electrode drying with water and

NMP. *Drying Technology* **2018**, *36* (2), 234–244. DOI: 10.1080/07373937.2017.1319855.

(21) Balzerowski, P.; Meister, K.; Versluis, J.; Bakker, H. J. Heterodyne-detected sum frequency generation spectroscopy of polyacrylic acid at the air/water-interface. *Physical chemistry chemical physics : PCCP* **2016**, *18* (4), 2481–2487. DOI: 10.1039/c5cp06177f.

(22) BÜCHI Labortechnik GmbH. *Spray drying*:*Optimizing the spray drying process*. https://www.buchi.com/en/spray-drying.

(23) Sovani, S.; Sojka, P.; Lefebvre, A. Effervescent atomization. *Progress in Energy and Combustion Science* **2001**, *27* (4), 483–521. DOI: 10.1016/S0360-1285(00)00029-0.

(24) Stähle, P.; Gaukel, V.; Schuchmann, H. P. Comparison of an Effervescent Nozzle and a Proposed A ir- C ore- L iquid- R ing (ACLR) Nozzle for Atomization of Viscous Food Liquids at Low Air Consumption. *J Food Process Engineering* **2017**, *40* (1). DOI: 10.1111/jfpe.12268.

(25) Zhou, H.; Pujales-Paradela, R.; Groppe, P.; Wintzheimer, S.; Mandel, K. Tuning the Morphology of Spray-Dried Supraparticles: Effects of Building Block Size and Concentration. *Part & Part Syst Charact* **2022**, *39* (11). DOI: 10.1002/ppsc.202200127.

(26) Park, S.; Hwang, H.; Kim, M.; Moon, J. H.; Kim, S.-H. Colloidal assembly in droplets: structures and optical properties. *Nanoscale* **2020**, *12* (36), 18576–18594. DOI: 10.1039/d0nr04608f. Published Online: Sep. 10, 2020.

(27) Lin, D.; Lu, Z.; Hsu, P.-C.; Lee, H. R.; Liu, N.; Zhao, J.; Wang, H.; Liu, C.; Cui, Y. A high tap density secondary silicon particle anode fabricated by scalable

mechanical pressing for lithium-ion batteries. *Energy Environ. Sci.* **2015**, *8* (8), 2371–2376. DOI: 10.1039/C5EE01363A.

(28) Pang, C.; Song, H.; Li, N.; Wang, C. A strategy for suitable mass production of a hollow Si@C nanostructured anode for lithium ion batteries. *RSC Adv.* **2015**, *5* (9), 6782–6789. DOI: 10.1039/C4RA10849C.

(29) Liu, T.-J.; Tiu, C.; Chen, L.-C.; Liu, D. The Influence of Slurry Rheology on Lithium-ion Electrode Processing. In *Printed batteries*:*Materials, technologies and applications*; Lanceros-Méndez, S., Costa, C. M., Eds.; John Wiley & Sons, Inc, 2018; pp 63–79. DOI: 10.1002/9781119287902.ch3.

(30) Komoda, Y.; Hira, T.; Kojo, H.; Miura, H.; Shibata, Y.; Udaka, K.; Watanabe, A.; Suzuki, K. The effect of yielding of dense silica slurry on the uniformity of coated layer. *J Coat Technol Res* **2022**, *19* (1), 61–72. DOI: 10.1007/s11998-021-00507-8.

(31) Yilmaz, M. T.; Vatansever, C. Three interval thixotropy test to determine structural regeneration of a glucomannan based hydrocolloid film at air/water interface: Interfacial, molecular, thermal and surface characterization. *Food Hydrocolloids* **2016**, *61*, 458–468. DOI: 10.1016/j.foodhyd.2016.06.004.

(32) Woodcock, L. V. Developments in the non-newtonian rheology of glass forming systems. In *Molecular Dynamics and Relaxation Phenomena in Glasses*; Caron, Williams, G., Dorfmüller, T., Eds.; Lecture Notes in Physics; Springer Verlag, 1987; pp 113–124. DOI: 10.1007/3-540-17801-5_7.

(33) Diehm, R.; Kumberg, J.; Dörrer, C.; Müller, M.; Bauer, W.; Scharfer, P.; Schabel, W. In Situ Investigations of Simultaneous Two-Layer Slot Die Coating of Component-Graded Anodes for Improved High-Energy Li-Ion Batteries. *Energy Tech* **2020**, *8* (5). DOI: 10.1002/ente.201901251.

(34) Haberzettl, P.; Filipovic, N.; Vrankovic, D.; Willenbacher, N. Processing of Aqueous Graphite–Silicon Oxide Slurries and Its Impact on Rheology, Coating Behavior, Microstructure, and Cell Performance. *Batteries* **2023**, *9* (12), 581. DOI: 10.3390/batteries9120581.

(35) Ramón-Torregrosa, P. J.; Rodríguez-Valverde, M. A.; Amirfazli, A.; Cabrerizo-Vílchez, M. A. Factors affecting the measurement of roughness factor of surfaces and its implications for wetting studies. *Colloids and Surfaces A: Physicochemical and Engineering Aspects* **2008**, *323* (1), 83–93. DOI: 10.1016/j.colsurfa.2007.10.032.

(36) Wu, B.; Quinn, J.; Li, J.; Li, Q.; Liu, D.; Martin, W.; Baar, K.; Zhong, L.; Wang, C.; Xiao, J. Understanding and Enhancing Silicon Nanoparticle Distribution during Electrode Processing. *J. Electrochem. Soc.* **2024**, *171* (5), 50542. DOI: 10.1149/1945-7111/ad4919.

(37) Wu, B.; Lu, W. Mechanical-Electrochemical Modeling of Agglomerate Particles in Lithium-Ion Battery Electrodes. *J. Electrochem. Soc.* **2016**, *163* (14), A3131-A3139. DOI: 10.1149/2.1331614jes.